A rigorous theoretical analysis of a surface-plasmon nanolaser with monolayer MoS_2 gain medium

XIANG MENG[1,*], RICHARD R. GROTE[2], WENCAN JIN[3], JERRY I. DADAP[1], NICOLAE C. PANOIU[4], AND RICHARD M. OSGOOD, JR.[1,3]

[1] Department of Electrical Engineering, Columbia University, New York, New York 10027
[2] Department of Electrical and Systems Engineering, University of Pennsylvania, Philadelphia, PA 19104
[3] Department of Applied Physics and Applied Mathematics, Columbia University, New York, New York 10027
[4] Department of Electronic and Electrical Engineering, University College London, Torrington Place, London WC1E 7JE, UK
[*] Corresponding author: meng@ee.columbia.edu

Compiled May 1, 2016

Lasers based on monolayer (ML) transition-metal dichalcogenide semiconductor crystals have the potential for low threshold operation and small device footprint; however, nanophotonic engineering is required to maximize interaction between optical fields and the three-atom-thick gain medium. Here, we develop a theoretical model to design a direct bandgap optically pumped nanophotonic integrated laser. Our device utilizes a gap-surface-plasmon optical mode to achieve subwavelength optical confinement and consists of a high-index GaP nanowire atop a ML MoS_2 film on a Ag substrate. The optical field and materials medium are analyzed using a three dimensional finite-difference time-domain (3D-FDTD) method and a first-principles calculation based on density functional theory (DFT), respectively. The nanolaser is designed to have a threshold of $\sim$0.6 μW under quasi-continuous wave operation on an excitonic transition at room temperature.

OCIS codes: *(140.3460) Lasers; (250.5403) Plasmonics; (160.4236) Nanomaterials; (130.3120) Integrated optics devices.*

http://dx.doi.org/10.1364/ao.XX.XXXXXX

The realization of an ultracompact subwavelength on-chip laser continues to be an unmet challenge for microdevice applications. However, this goal has recently been advanced with devices based on the plasmonic properties of metals, which confine optical excitation to subwavelength dimensions *via* surface plasmon polaritons (SPPs) at metal-dielectric interfaces [1–4]. When coupled to a suitable optical gain medium, SPP lasers can achieve tight plasmonic (optical) confinement and feedback, which reduces the optical mode volume far below the scale of a vacuum wavelength. The ability to confine optical energy to such small volumes offers an ideal platform for coupling to the unique material properties of gain media with reduced dimensionality.

For these lasers, monolayers of transition-metal dichalcogenide semiconductors (TMDCs) present a number of desirable electronic and optical properties for use as a gain medium, such as a relatively large direct bandgap, robust excitons, and strong photoluminescence (PL). For example, molybdenum disulfide (MoS_2) has a direct gap of 1.82 eV, when the thickness of a bulk crystal is decreased to a ML. This ML form of MoS_2 has a luminescence quantum efficiency of more than a factor 10^4 greater than the bulk crystal [5]. More importantly, it has a sufficiently large binding energy to be stable at room temperature. The combination of these electrical and optical properties, which are not seen in crystals other than ML TMDC, makes them promising candidates for novel optoelectronic devices, such as light-emitting devices operating in the visible range [6–9].

In this paper, we report the design of an optically pumped plasmonically excited TMDC laser using a rigorous theoretical analysis. The analysis is based on a fully three-dimensional finite element method (FEM) mode solver, finite-difference time-domain (3D-FDTD) computation for the time varying optical fields, and a first-principles calculation using density functional theory (DFT) for examining excitonic optical transition in mate-

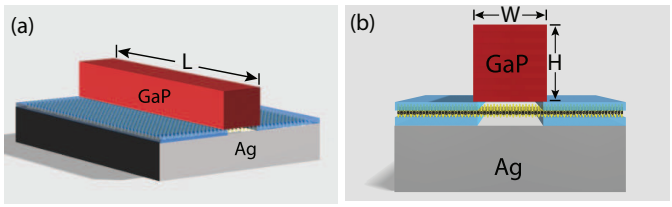

Fig. 1. (a) Perspective view of the nanolaser structure: on a metallic substrate (Ag), the nanowire (GaP) of length L ~1 μm seats on a pair of slotted spacer layers SiO_2 (blue layer) embedding the ML semiconductor film (MoS_2) that acts as the active medium. (b) Cross-sectional view of the device structure, showing that the width (W) and height (H) of ~0.2 μm for nanowire.

rial medium [10].

The nanolaser topology analyzed here is illustrated in Fig. 1. The device uses a ML of MoS_2 factive medium and a deep-subwavelength dimension cavity. This cavity, which is approximately 1 µm long, provides resonances within the surface plasmon spectral bandwidth. This structure uses the 2D nature of the ML of the MoS_2, along with its overlaying and underlaying dielectric and plasmonic layers to obtain a low-threshold behavior. This geometry also includes a high-refractive-index nanowire (GaP, $n = 3.2$) placed on top of a low-refractive-index (SiO_2, $n = 1.45$) thin films that sandwich the MoS_2, near the atomically smooth metal (Ag) film surface [2] that serves as a surface plasmon polariton (SPP) waveguide. Silver is used due to its minimal plasmonic damping at the visible and near-infrared wavelength range. The laser design incorporates a slot in the SiO_2 layer so as to form region of suspended MoS_2 and hence reduced carrier loss; this reduced carrier recombination lifetime is known to lead, for example, to stronger photoluminescence [11]. GaP is chosen because of its higher refractive index and large bandgap, which yields a higher group index of 4.5 and reduces optical absorption and thus helps to reduce the lasing threshold [12, 13]. The SPP scattering due to surface roughness [14] and grain boundaries [15] are ignored in our analysis. The finite length of the nanowire defines the cavity that laterally confines cavity modes in the gap between the nanowire and SPP waveguide, with cavity feedback arising from modal reflection at the end-facets. The suspended MoS_2 on the spacer slot can be fabricated using standard transfer techniques [16]. The semiconductor nanowire can be carefully patterned using, for example, AFM lithography [17]. The MoS_2 has a finite thickness of 0.7 nm with a measured refractive index of $5.76+i1.13$ [18]. The nanolaser has a length of 0.996 µm, which is carefully chosen by FDTD analysis that will be discussed in detail in a later section. Other ML TMDC materials have even higher quantum yield, such as WS_2 and WSe_2 [10], however, here we analyze the case of ML MoS_2 since it has well-characterized set of experimental material parameters.

To obtain a basic theoretical understanding of the time-evolution of the lasing behavior, we use the following rate-equation approach [19]:

$$\frac{dN}{dt} = R - \frac{N}{\tau_r} - \frac{N}{\tau_{nr}} - v_g g(N - N_{tr})P \quad \textbf{(1)}$$

$$\frac{dP}{dt} = \Gamma v_g g(N - N_{tr})P + \Gamma\beta\frac{N}{\tau_r} - \frac{P}{\tau_c} \quad \textbf{(2)}$$

where N and P are the carrier and photon densities within the nanocavity, R is the pumping rate, v_g is the group velocity obtained by calculating the group index, which is related to the derivative of phase index obtained from finite element methods, g is the differential gain coefficient, $\partial\gamma/\partial N$, where γ is the gain and N_{tr} is the transparency carrier density, the number of carriers that must be excited to the upper state to render the medium transparent. The cavity photon lifetime, the radiative, and the nonradiative recombination lifetimes are τ_c, τ_r and τ_{nr}, respectively [20]. The spontaneous emission factor, β, is defines as the fraction of the spontaneous emission radiated into the cavity mode. The overlap factor, Γ, accounts for the matching between the active region and the optical mode. In the following analysis, FEM is used to find the modal group velocity and the modal overlap with the gain medium, DFT is used to find the differential gain coefficient, and FDTD is used to find the cavity losses and spontaneous emission factor.

In addition, we show that the cavity mode can be described as a superposition of the waveguide mode and the SPP mode, i.e., a hybrid mode, using using coupled-mode theory [21]:

$$\Psi = a\Psi_{wg} + b\Psi_{spp} \quad \textbf{(3)}$$

where a and b are the amplitudes of the constituent waveguide $\Psi_{wg} = \{1\,0\}^T$ and SPP $\Psi_{spp} = \{0\,1\}^T$ basis modes, respectively. The modes of the coupled system are characterized by the system of equations discussed in [22]

$$\begin{pmatrix} n_{wg} & \kappa_{12} \\ \kappa_{21} & n_{spp} \end{pmatrix} \begin{pmatrix} a \\ b \end{pmatrix} = n_{eff} \begin{pmatrix} a \\ b \end{pmatrix} \quad \textbf{(4)}$$

where κ_{12}, κ_{21} are the waveguide coupling parameters (calculated by solving the overlap integral), n_{wg} and n_{spp} are the refractive index of waveguide and the effective index of SPP waveguide, respectively, and n_{eff} is the effective index of this hybrid mode. The analytical solution of Eq. 4 further serves as a check to the numerical calculations described below. In fact, the results of two methods agree completely with each other.

A cross-section of the device, with an overlay of a plot of the hybrid gap mode, calculated by FEM, is shown in Fig. 2(a). The strong plasmonic confinement enables ultratight vertical localization of the hybrid optical mode. Further as is seen in Fig. 2, the hybrid mode is also tightly confined in the transverse direction by the GaP nanowire; thus both effects result in excellent spatial overlap between the mode and the ML gain medium and enabling the ultralow-threshold CW lasing operation in a diffraction-free footprint. The nanowire geometry was designed to maximize the field in the ML of MoS_2, so as also to maximize the absorption efficiency of ML MoS_2. The layer of SiO_2 serves as a low-permittivity spacer that leads to a strong normal electric field component due to the continuity of the displacement field across this interface. In addition, such a low-index dielectric-metal interface also leads to low propagation loss. The overlayer nanowire "guides" the hybrid gap mode, where its reflectivity depends only on the mismatch between the effective index of the structure and the free space.

Due to the 2D nature of the MoS_2 (semiconductor) ML, the band structure of a suspended ML behaves as a quantum well, with an effective out-of-plane potential, which can be calculated using density-functional-theory ABINIT code under the generalized gradient approximation [23]. In this calculation, a periodic slab geometry with a 12 Å vacuum layer is used. In addition, the in-plane lattice constant and the interplane distance between the Mo and S atomic planes are structurally optimized. The calculation employs a $10 \times 10 \times 1$ k-point mesh with a wave function cut-off energy of 50 *Hartree* and an energy difference tolerance of

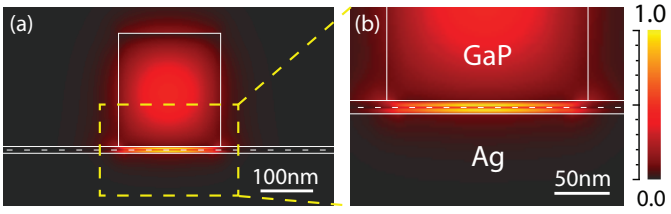

Fig. 2. (a) The hybrid-mode profile of the combined nanowire and SPP waveguide modes. (b) An enlarged region from panel (a) showing the gap mode and the MoS_2 monolayer (white dashed line).

10^{-10}. Due to this quantum-well structure, ML TMDCs should offer some of the well known advantages of more conventional quantum well lasers, namely, the large differential gain associated with their 2D density of states. Moreover, compared to conventional group III-V quantum well lasers, the large refractive index of ML TMDCs can significantly increase the optical confinement in the laser active region of the laser. The optical gain can be further enhanced by the strong Colulombic interactions, due to the vertical confinement and the reduced dielectric screening [24].

These points are shown in a more detailed manner by the bandstructure of MoS_2. Thus Fig. 3(a) shows the calculated effective potential profile of ML MoS_2 along the out-of-plane direction (c axis). This potential profile indicates that in ML MoS_2, the pure in-plane nature of the electrons due to quantum confinement can be described by a single quantum-well model, which has a significant but finite barrier (8 eV) to electron transport in the out of plane direction. This barrier fully confines the gain of an optical wave within the quantum-well crystal medium. Figure 3(b) shows the uppermost valence band and the excitonic band along $\bar{\Gamma}$-$\bar{K}$-$\bar{M}$-$\bar{\Gamma}$ high-symmetry line. The figure shows a direct band gap of 1.82 eV at $\bar{K}$, which is very close to the experimental result given in [5]. Note the band splitting due to spin-orbit is not considered here because the linear polarized excitation wave will excite both spin-up and spin-down electrons. By fitting the valence band maximum (VBM) and excitonic band minimum (EBM) in the vicinity of $\bar{K}$ to a parabola, the hole effective mass can be extracted at the VBM ($m_v = 0.61m_e$) and the electron effective mass at the EBM ($m_c = 0.51m_e$), respectively. The carrier effective masses in our calculation are in good agreement with the values determined by G_0W_0 calculations [25]. It is worth noting that the relatively large effective masses of charge carriers in MoS_2 results in high densities of states in both the valence and conduction bands. This fact, coupled with the fairly large bandgap of MoS_2, requires carrier concentrations of $\sim 1 \times 10^{19}$ cm^{-3} to push the quasi-Fermi levels into the corresponding bands so as to achieve population inversion. A recent experiment reported has confirmed the presence of such high carrier concentrations [26].

The quantum-well behavior of the effective potential profile together with the carrier effective mass allow calculation of gain, where its analytic form at excitation frequency ω_0 is [27]

$$\gamma(\omega_0) = \frac{m_r \lambda_0^2}{4\pi\hbar L_z n^2 \tau}[f_c(\hbar\omega_0) - f_v(\hbar\omega_0)] \quad (5)$$

where L_z is the thickness, τ is the recombination lifetime, n is the refractive index of ML active medium and where continuous wave operation is assumed. The gain coefficient also depends on the excitation wavelength λ_0, the reduced mass m_r, as well as the quasi-Fermi functions f_c and f_v that are evaluated at room temperature. Attainment of a low optical threshold is an important practical aspect of plasmonically enhanced lasers, such as the one studied here, since it governs the minimum power consumption that is necessary for useful device operation. In this paper, the lasing threshold is defined by equating optical gain in the medium to the losses in the laser structure. Using a steady-state solution to the coupled rate equations, a relationship between pumping rate R and photon densities P is obtained.

Designing the cavity requires consideration of different factors. The overlap factor, $\Gamma = \int_{gain} \epsilon_g E^2 dv / \int_{cavity} \epsilon_c E^2 dv$, which is the overlap volume integral of the gain medium with the cavity mode, and E is the electric filed, ϵ_g and ϵ_c are the dielectric constants of the gain medium and cavity, respectively. For example, Fig. 4(a) shows the calculated overlap factor as a function of the gap thickness. The "error" bars in this figure are in fact ranges of overlap factor at each gap thickness generated by varying the nanowire geometry over different height and width combinations from 140 nm to 220 nm respectively. The different combinations of dimensions can successfully support the fundamental mode with essentially very little energy leakage. Note the gap thickness controls sensitively the optical confinement thus the laser threshold and the practical limitations in fabricating the laser structure also influence the actual design. For example, a perfect gap size of less than 5 nm yields a low laser threshold due to high confinement, but it is a challenge in fabrication, as a result, we have chosen to use a larger gap thickness of 7 nm. This dimension yields a satisfactory $\Gamma \approx 11\%$.

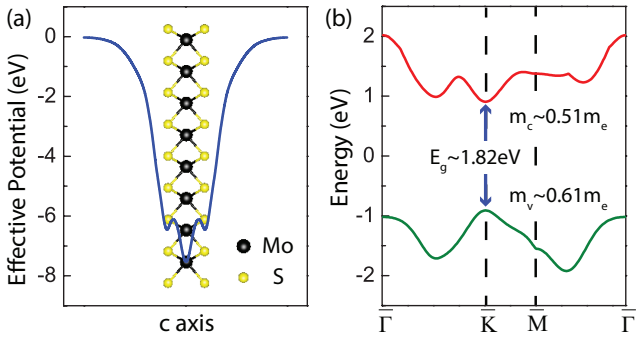

Fig. 3. (a) The effective potential profile of the suspended monolayer MoS_2 that behaves like a quantum-well with a finite barrier of 8eV. (b) The electron band structure of suspended monolayer MoS_2 with a bandgap of 1.82eV.

Second, plasmonic and radiative loss must be examined. Thus, the condition for laser oscillation at laser threshold is achieved when the sum of all losses, α, including physical processes, such as ohmic loss in the metal, emission of SPPs to outside of the cavity, radiation leakage into the substrate, and far-field emission, is exactly balanced by the gain of the laser medium, γ. The loss factor can be expressed as $\alpha = \omega_r/(v_g Q)$ with ω_r as the optical frequency at cavity resonance and Q is the quality factor. Hence minimizing the cavity loss entails optimizing Q, which is obtained by making use of RSoft Q-finder tool, a 3D-FDTD based software [28]. For this calculation, we use a laser wavelength of $\lambda = 682$nm, which is the free-space emission wavelength of ML MoS_2. We optimized the cavity length to be 0.996 µm for maximum $Q = 91.7$ at a wavelength near the bandgap of Mos_2, a value comparable to that reported in [2, 13]. This Q is relatively low compared to typical diode lasers due to the low reflectivity at each of the interface facet. Note that a small variation in nanowire length will shift Q downwards [29], thus yielding an increase in laser threshold. However using the literature values for dimensional tolerance on fabrication structures such as this, we believe that relatively high Q values can be obtained for our sources. Meanwhile, the extremely small mode volume and correspondingly the Purcell enhancement, are Q/V_m, compensates for the modest Q. In particular, the mode volume V_m in our design is found to be $\sim \lambda^3/380$ via numerical computation. This small mode volume results in the large Purcell factor, $F = (3/4\pi^2)(Q/V_m)(\lambda/n_{eff})^3$, with a value of 118.3 for this specific design. Lasing at a reduced threshold power is achieved by enhancing spontaneous emission rate via the Purcell factor, thus leading to an enhanced stimulated emission rate.

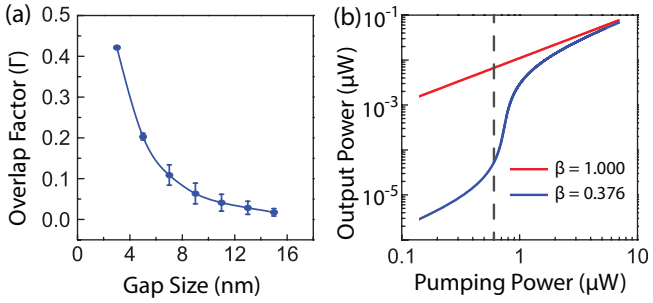

Fig. 4. (a) Effect of different gap size on the overlap factor, Γ. (b) Nonlinear pump curve versus pumping factor for different spontaneous emission factors $\beta = 0.376$ and 1 for the real structure and the ideal thresholdless case respectively.

The third phenomenon is the spontaneous emission factor β. Its generic equation is based on a "one photon per mode" picture [30] and is defined as

$$\beta(\vec{r},\omega) = \frac{\langle|\vec{\mu}\cdot\vec{E}_{cav}(\vec{r},\omega)|^2\rangle}{\sum_i \langle|\vec{\mu}\cdot\vec{E}_i(\vec{r},\omega)|^2\rangle} \quad (6)$$

where $|\vec{E}_{cav}(\vec{r},\omega)|^2$ represents the vacuum-field density in the cavity mode at atomic position $\vec{r}$ with frequency ω and where the sum in the denominator runs over all modes with $\vec{\mu}\cdot\vec{E}_i$ as dipolar atom-field interaction Hamiltonian. The device is assumed to work at a constant temperature; thus the temperature dependence of β is ignored. By setting the loss of the laser structure, α, equal to the gain of lasing medium, γ, we calculate the population of optically generated electron-hole pairs ΔN required to reach laser threshold, which is on the order of $10^{19} cm^{-3}$ and therefore this population inversion can be used to obtain the corresponding nonlinear light pump curve containing the spontaneous emission factor $\beta = 0.376$. This curve, shown in Fig. 4(b), gives a lasing threshold of 0.62 μW at 300 K, which is comparable to that of other nanolasers [7, 10, 26].

Finally note that, in addition to the above approach to the nanolaser, there are several variations in the design that may further improve the device performance. For example, the use of a photonic crystal waveguide will provide a potentially much larger group index, a property which will lead to slow-light [31] enhancement of the circulating field and better confinement, thus further reducing the lasing threshold.

In summary, we have demonstrated a new nanolaser design using a 2D TMDC material as the active medium. We have also examined the lasing threshold requirements based on optically pumped surface-plasmon excitation. A nanowire is used to concentrate the light effectively into 2D active medium. The resulting highly confined hybrid mode allows for subdiffraction-limited localization of electromagnetic-field-energy density at the interface of a metal substrate and a high-dielectric-constant slab, enabling a low-threshold, compact integrated laser source.

Acknowledgment. The simulations were performed on the computer cluster in the Center for Functional Nanomaterials (CFN) at the Brookhaven National Laboratory (BNL), which is supported by the U.S. Department of Energy, Office of Basic Energy Sciences, under Contract No. DE-AC02-98CH10886. We also thank Steven Brueck, Aron Pinczuk, Nathaniel Osgood for insightful discussion during the research as well as Mayank Bahl of RSoft for an on-going discussion of the simulation methods used here. N. C. P. acknowledges support from European Research Council / ERC Grant Agreement no. ERC-2014-CoG-648328.

REFERENCES

1. D. J. Bergman and M. I. Stockman, Phys. Rev. Lett.**90**, 027402 (2003).
2. Y.-J. Lu, J. Kim, H.-Y. Chen, C. Wu, N. Dabidian, C. E. Sanders, C.-Y. Wang, M.-Y. Lu, B.-H. Li, X. Qiu, W.-H. Chang, L.-J. Chen, G. Shvets, C.-K. Shih and S. Gwo, Science **337**, 450 (2012).
3. R. F. Oulton, V. J. Sorger, T. Zentgraf, R.-M. Ma, C. Gladden, L. Dai, G. Bartal, and X. Zhang, Nature (London) **461**, 629 (2009).
4. X. Meng, R. R. Grote, J. I. Dadap, N. C. Panoiu, and R. M. Osgood, Opt. Express **22**, 22018 (2014).
5. K. F. Mak, C. Lee, J. Hone, J. Shan, and T. F. Heinz, Phys. Rev. Lett.**105**, 136805 (2010).
6. K. M. Goodfellow, R. Beams, C. Chakraborty, L. Novotny, and A. N. Vamivakas, Optica**1**, 149 (2014).
7. S. Wu, S. Buckley, J. R. Schaibley, L. Feng, J. Yan, D. G. Mandrus, F. Hatami, W. Yao, J. Vučković, A. Majumdar and X. Xu, Nature (London) **520**, 69 (2015).
8. R. S. Sundaram, M. Engel, A. Lombardo, R. Krupke, A. C. Ferrari, P. Avouris, and M. Steiner, Nano Lett. **13**, 1416 (2013).
9. X. Meng, R. Grote, J. Dadap, and R. Osgood, "Threshold analysis in monolayer semiconductor nanolaser by surface plasmon enhancement," in "Laser Science," (Optical Society of America, 2015), pp. LTh3I–3.
10. Y. Ye, Z. J. Wong, X. Lu, X. Ni, H. Zhu, X. Chen, Y. Wang, and X. Zhang, Nature Photon. **9**, 733 (2015).
11. H. Shi, R. Yan, S. Bertolazzi, J. Brivio, B. Gao, A. Kis, D. Jena, H. G. Xing, and L. Huang, ACS Nano. **7**, 1072 (2013).
12. M. Z. Alam, J. S. Aitchison, and M. Mojahedi, Laser Photon. Rev. **8**, 394 (2014).
13. Y.-J. Lu, C.-Y. Wang, J. Kim, H.-Y. Chen, M.-Y. Lu, Y.-C. Chen, W.-H. Chang, L.-J. Chen, M. I. Stockman, C.-K. Shih and S. Gwo, Nano letters **14**, 4381 (2014).
14. L. Cao, N. Panoiu, R. D. Bhat, and R. Osgood Jr, Phys. Rev. B **79**, 235416 (2009).
15. D. McLean and A. Maradudin, Phys. Today **11**, 35 (2009).
16. W. Jin, P.-C. Yeh, N. Zaki, D. Zhang, J. T. Liou, J. T. Sadowski, A. Barinov, M. Yablonskikh, J. I. Dadap, P. Sutter, I. P. Herman and R. Osgood Jr, Phys. Rev. B **91**, 121409 (2015).
17. X. Xie, H. Chung, C. Sow, and A. Wee, Mater. Sci. Eng. **54**, 1 (2006).
18. A. Castellanos-Gomez, N. Agrait, and G. Rubio-Bollinger, Appl. Phys. Lett. **96**, 213116 (2010).
19. L. A. Coldren, S. W. Corzine, and M. L. Mashanovitch, *Diode lasers and photonic integrated circuits*, vol. 218 (John Wiley & Sons, 2012).
20. T. Korn, S. Heydrich, M. Hirmer, J. Schmutzler, and C. Schuller, Appl. Phys. Lett. **99**, 102109 (2011).
21. H. A. Haus, *Waves and fields in optoelectronics*, vol. 464 (Prentice-Hall Englewood Cliffs, NJ, 1984).
22. R. F. Oulton, V. J. Sorger, D. Genov, D. Pile, and X. Zhang, Nature Photon. **2**, 496 (2008).
23. X. Gonze, Zeitschrift für Kristallographie **220**, 558 (2005).
24. J. Yao, G. P. Agrawal, and P. Gallion, IEEE Photon. Technol. Lett. **7**, 149 (1995).
25. A. Ramasubramaniam, Phys. Rev. B **86**, 115409 (2012).
26. O. Salehzadeh, M. Djavid, N. H. Tran, I. Shih, and Z. Mi, Nano Lett. **15**, 5302 (2015).
27. A. Yariv and P. Yeh, *Photonics: Optical Electronics in Modern Communications* (Oxford University Press, 2006).
28. C. RSoft, Inc., RSoft Products (2014).
29. L. Carletti, A. Locatelli, O. Stepanenko, G. Leo, and C. De Angelis, Opt. Lett. **23**, 26544 (2015).
30. M. Van Exter, G. Nienhuis, and J. Woerdman, Phys. Rev. A **54**, 3553 (1996).
31. J. F. McMillan, X. Yang, N. C. Panoiu, R. M. Osgood, and C. W. Wong, Opt. Lett. **31**, 1235 (2006).

FULL REFERENCES

1. D. J. Bergman and M. I. Stockman, "Surface plasmon amplification by stimulated emission of radiation: Quantum generation of coherent surface plasmons in nanosystems," Phys. Rev. Lett.**90**, 027402 (2003).
2. Y.-J. Lu, J. Kim, H.-Y. Chen, C. Wu, N. Dabidian, C. E. Sanders, C.-Y. Wang, M.-Y. Lu, B.-H. Li, X. Qiu *et al.*, "Plasmonic nanolaser using epitaxially grown silver film," Science **337**, 450–453 (2012).
3. R. F. Oulton, V. J. Sorger, T. Zentgraf, R.-M. Ma, C. Gladden, L. Dai, G. Bartal, and X. Zhang, "Plasmon lasers at deep subwavelength scale," Nature (London) **461**, 629–632 (2009).
4. X. Meng, R. R. Grote, J. I. Dadap, N. C. Panoiu, and R. M. Osgood, "Engineering metal-nanoantennae/dye complexes for maximum fluorescence enhancement," Opt. Express **22**, 22018–22030 (2014).
5. K. F. Mak, C. Lee, J. Hone, J. Shan, and T. F. Heinz, "Atomically thin mos_2: A new direct-gap semiconductor," Phys. Rev. Lett.**105**, 136805 (2010).
6. K. M. Goodfellow, R. Beams, C. Chakraborty, L. Novotny, and A. N. Vamivakas, "Integrated nanophotonics based on nanowire plasmons and atomically thin material," Optica**1**, 149–152 (2014).
7. S. Wu, S. Buckley, J. R. Schaibley, L. Feng, J. Yan, D. G. Mandrus, F. Hatami, W. Yao, J. Vučković, A. Majumdar *et al.*, "Monolayer semiconductor nanocavity lasers with ultralow thresholds," Nature (London) **520**, 69–72 (2015).
8. R. S. Sundaram, M. Engel, A. Lombardo, R. Krupke, A. C. Ferrari, P. Avouris, and M. Steiner, "Electroluminescence in single layer mos2," Nano Lett. **13**, 1416–1421 (2013).
9. X. Meng, R. Grote, J. Dadap, and R. Osgood, "Threshold analysis in monolayer semiconductor nanolaser by surface plasmon enhancement," in "Laser Science," (Optical Society of America, 2015), pp. LTh3I–3.
10. Y. Ye, Z. J. Wong, X. Lu, X. Ni, H. Zhu, X. Chen, Y. Wang, and X. Zhang, "Monolayer excitonic laser," Nature Photon. **9**, 733–737 (2015).
11. H. Shi, R. Yan, S. Bertolazzi, J. Brivio, B. Gao, A. Kis, D. Jena, H. G. Xing, and L. Huang, "Exciton dynamics in suspended monolayer and few-layer mos2 2d crystals," ACS Nano. **7**, 1072–1080 (2013).
12. M. Z. Alam, J. S. Aitchison, and M. Mojahedi, "A marriage of convenience: Hybridization of surface plasmon and dielectric waveguide modes," Laser Photon. Rev. **8**, 394–408 (2014).
13. Y.-J. Lu, C.-Y. Wang, J. Kim, H.-Y. Chen, M.-Y. Lu, Y.-C. Chen, W.-H. Chang, L.-J. Chen, M. I. Stockman, C.-K. Shih *et al.*, "All-color plasmonic nanolasers with ultralow thresholds: autotuning mechanism for single-mode lasing," Nano Lett. **14**, 4381–4388 (2014).
14. L. Cao, N. Panoiu, R. D. Bhat, and R. Osgood Jr, "Surface second-harmonic generation from scattering of surface plasmon polaritons from radially symmetric nanostructures," Phys. Rev. B **79**, 235416 (2009).
15. D. McLean and A. Maradudin, "Grain boundaries in metals," Phys. Today **11**, 35–36 (2009).
16. W. Jin, P.-C. Yeh, N. Zaki, D. Zhang, J. T. Liou, J. T. Sadowski, A. Barinov, M. Yablonskikh, J. I. Dadap, P. Sutter *et al.*, "Substrate interactions with suspended and supported monolayer mo s 2: Angle-resolved photoemission spectroscopy," Phys. Rev. B **91**, 121409 (2015).
17. X. Xie, H. Chung, C. Sow, and A. Wee, "Nanoscale materials patterning and engineering by atomic force microscopy nanolithography," Mater. Sci. Eng. **54**, 1–48 (2006).
18. A. Castellanos-Gomez, N. Agrait, and G. Rubio-Bollinger, "Optical identification of atomically thin dichalcogenide crystals," Appl. Phys. Lett. **96**, 213116 (2010).
19. L. A. Coldren, S. W. Corzine, and M. L. Mashanovitch, *Diode lasers and photonic integrated circuits*, vol. 218 (John Wiley & Sons, 2012).
20. T. Korn, S. Heydrich, M. Hirmer, J. Schmutzler, and C. Schuller, "Low-temperature photocarrier dynamics in monolayer mos[sub 2]," Appl. Phys. Lett. **99**, 102109 (2011).
21. H. A. Haus, *Waves and fields in optoelectronics*, vol. 464 (Prentice-Hall Englewood Cliffs, NJ, 1984).
22. R. F. Oulton, V. J. Sorger, D. Genov, D. Pile, and X. Zhang, "A hybrid plasmonic waveguide for subwavelength confinement and long-range propagation," Nature Photon. **2**, 496–500 (2008).
23. X. Gonze, "A brief introduction to the abinit software package," Zeitschrift für Kristallographie **220**, 558–562 (2005).
24. J. Yao, G. P. Agrawal, and P. Gallion, "Linewidth enhancement factor and nonlinear gain in znse semiconductor lasers," IEEE Photon. Technol. Lett. **7**, 149–151 (1995).
25. A. Ramasubramaniam, "Large excitonic effects in monolayers of molybdenum and tungsten dichalcogenides," Phys. Rev. B **86**, 115409 (2012).
26. O. Salehzadeh, M. Djavid, N. H. Tran, I. Shih, and Z. Mi, "Optically pumped two-dimensional mos2 lasers operating at room-temperature," Nano Lett. **15**, 5302–5306 (2015).
27. A. Yariv and P. Yeh, *Photonics: Optical Electronics in Modern Communications* (Oxford University Press, 2006).
28. C. RSoft, "User guide, synopsys," Inc., RSoft Products (2014).
29. L. Carletti, A. Locatelli, O. Stepanenko, G. Leo, and C. De Angelis, "Enhanced second-harmonic generation from magnetic resonance in algaas nanoantennas," Opt. Lett. **23**, 26544–26550 (2015).
30. M. Van Exter, G. Nienhuis, and J. Woerdman, "Two simple expressions for the spontaneous emission factor β," Phys. Rev. A **54**, 3553 (1996).
31. J. F. McMillan, X. Yang, N. C. Panoiu, R. M. Osgood, and C. W. Wong, "Enhanced stimulated raman scattering in slow-light photonic crystal waveguides," Opt. Lett. **31**, 1235–1237 (2006).